

Tidal disruption of satellites and formation of narrow rings

Zoë M. Leinhardt^{1,2*}, Gordon I. Ogilvie¹, Henrik N. Latter¹, and Eiichiro Kokubo³

¹*Department of Applied Mathematics and Theoretical Physics, University of Cambridge, Cambridge CB3 0WA*

²*School of Physics, University of Bristol, BS8 1TL*

³*National Astronomical Observatory of Japan, 2-21-1 Osawa, Mitaka, Tokyo 181-8588, Japan*

Accepted 2012 May 16. Received 2012 May 16; in original form 2012 March 28

ABSTRACT

In this paper we investigate the formation of narrow planetary rings such as those found around Uranus and Saturn through the tidal disruption of a weak, gravitationally bound satellite that migrates within its Roche limit. Using N -body simulations, we study the behaviour of rubble piles placed on circular orbits at different distances from a central planet. We consider both homogeneous satellites and differentiated bodies containing a denser core. We show that the Roche limit for a rubble pile is closer to the planet than for a fluid body of the same mean density. The Roche limit for a differentiated body is also closer to the planet than for a homogeneous satellite of the same mean density. Within its Roche limit, a homogeneous satellite totally disrupts and forms a narrow ring. The initial stages of the disruption are similar to the evolution of a viscous fluid ellipsoid, which can be computed semi-analytically. On the other hand, when a differentiated satellite is just within the Roche limit only the mantle is disrupted. This process is similar to Roche-lobe overflow in interacting binary stars and produces two narrow rings on either side of a remnant satellite. We argue that the Uranian rings, and possibly their shepherd satellites, could have been formed through the tidal disruption of a number of protomoons that were formed inside the corotation radius of Uranus and migrated slowly inwards as a result of tidal interaction with the planet.

1 INTRODUCTION

This paper is the first in a series investigating the formation and evolution of planetary rings. The outer planets of the solar system harbour ring systems of surprising diversity. Although they have been explored through space missions as well as ground-based observations, and Saturn's rings are currently being imaged with unprecedented resolution by the *Cassini* spacecraft, fundamental questions still remain about the formation and evolution of planetary rings.

There are four main hypotheses for the formation of the ring systems: (i) the rings are primordial and were formed directly from the circumplanetary disk (Pollack 1975; Charnoz et al. 2009); (ii) the rings were formed subsequently from a satellite that was disrupted by an impact within the Roche limit of the planet (Harris 1984; Charnoz et al. 2009); (iii) the rings were formed from the tidal disruption of a satellite that migrated within the Roche limit (Canup 2010); (iv) the rings were formed by the tidal disruption of a passing comet (Dones 1991). Of course it is possible that more than one formation mechanism is responsible for the various ring systems.

The study of planetary rings is important not only to explain their remarkable structure today but also because the history of the rings may be intimately connected to the formation and evolution of the planet. If the ring systems can be interpreted correctly, a considerable amount may be learned about their host planets. In addition, planetary rings

give us the opportunity to make a detailed study of the behaviour of astrophysical disks and their interaction with satellites, processes that are important in settings that range from protoplanetary systems to galactic nuclei.

In this series of papers we will focus on the narrow, dense rings of Uranus, although similar rings are also found at certain locations around Saturn (including the F ring, although its proximity to the Roche limit may make it a separate case). The present paper is concerned with the formation of narrow rings, while subsequent work will treat their dynamics and evolution. Narrow, dense rings have received relatively little attention and offer many theoretical puzzles. They are the main constituents of the Uranian ring system, where they are usually assumed to be shepherded by small satellites. Narrow rings are typically eccentric and inclined, and may contain other nonlinear oscillation modes (Porco 1990). Questions abound concerning the formation of narrow rings, their present confinement by shepherd satellites or other mechanisms, the assembly and evolution of shepherding configurations, the lifetime of narrow rings, the origin of their eccentricity, inclination and other oscillation modes, and so on.

The Uranian system has 13 known rings (Showalter & Lissauer 2006), three of which (ζ , μ and ν) are broad dust rings and will not be considered here. The low geometric albedo of the Uranian rings, which makes them difficult to detect, indicates that their composition

includes at least some dark material (Ockert et al. 1987; Karkoschka 1997). Most of the narrow rings themselves are effectively devoid of dust particles, having particle radii between 0.1 and 10 m (Esposito et al. 1991). The λ ring is the exception and is composed of sub- μm and μm -sized dust particles (Showalter 1993; Burns et al. 2001). The rings are either optically thick or close to it (e.g. Karkoschka 2001b) and very narrow with typical widths of a few km. It is assumed that the lack of small dust particles is due to aerodynamic gas drag from the extended Uranian exosphere (Broadfoot 1986).

There are many questions about the Uranian ring system that remain to be answered: (i) How did the rings form? (ii) How old are the rings? (iii) How are the rings' narrow width and sharp edges maintained? It is possible that all the narrow rings (6, 5, 4, α , β , η , γ , δ , λ , and ϵ) are shepherded by small satellites. However, only two potential shepherds (Cordelia and Ophelia) have been detected, located on either side of the ϵ ring. We will address the spreading and confinement of narrow rings in future work.

The most accepted formation model for the Uranian rings is a series of disruptive collisions of pre-existing satellites (Esposito 2006). However, this model does not explain why most of the rings are interior to the known satellites. In this paper we suggest that it is more likely that satellites were tidally disrupted as they migrated within the Roche limit. Tidal disruption has also been suggested for the formation of the Saturnian ring system. Canup (2010) proposed that the partial mantle disruption of a large Titan-sized satellite could explain many properties of the rings including their composition of nearly pure water ice. The gas disk surrounding Saturn early in its history causes the satellite to migrate within its Roche limit and be partially disrupted, with the remnant satellite and a significant fraction of the ring material being consumed by Saturn. Here we suggest that each narrow ring in the Uranian system could have resulted from the complete or partial tidal disruption of a single small satellite. Unlike Canup (2010), we do not require the tidal disruption to occur early in the history of Uranus when a gas disk is present. In the Uranian system the corotation radius is well outside the Roche limit for a homogenous fluid satellite with a density similar to that of water ice, so the inner satellites migrate inwards as a result of tidal dissipation within Uranus.

The timescale of orbital migration driven by tidal dissipation within Uranus can be written as

$$\tau_a = \frac{2}{13} \frac{a}{|\dot{a}|} = \frac{4}{117} \frac{M_U}{M_s} \left(\frac{a}{R_U} \right)^5 \frac{Q'_U}{n}, \quad (1)$$

where a is the orbital semimajor axis, n is the orbital mean motion, M_U and R_U are the mass and radius of Uranus, M_s the mass of the satellite and Q'_U is the reduced tidal quality factor of Uranus at the relevant tidal frequency (Goldreich & Soter 1966). The migration is inward for satellites orbiting inside the corotation radius of the planet and outward for satellites outside corotation. The factor of 2/13 reflects the accelerating nature of inward migration and gives the time for complete orbital decay under the assumption of constant Q'_U . It is a remarkable fact that τ_a is on the order of $10^5 Q'_U$ yr for many of the small inner satellites (including Cordelia and Ophelia) that orbit inside the corotation radius as well as for Mi-

randa and Ariel (which are outside corotation), despite the wide range of masses of these satellites. Furthermore, all the regular satellites except Cordelia exert tidal forcing on Uranus at a frequency at which inertial waves can be excited, assuming that Uranus is uniformly rotating (Ogilvie & Lin 2004). Based on evolutionary scenarios for Miranda, Umbriel and Ariel using a frequency-independent tidal quality factor, Tittlemore & Wisdom (1990) have argued¹ that Q'_U lies between 1.6×10^5 and 5.6×10^5 , most likely towards the low end of this range. Although Q'_U is unlikely to be frequency-independent, values in this range would allow significant inward migration of the smaller inner moons, as well as significant outward migration of Miranda and Ariel, over the age of the solar system.

In order to study tidal disruption and the formation of narrow rings we have designed a series of numerical simulations. In these simulations a small satellite, either homogeneous or differentiated, is placed in a circular orbit in the gravitational potential of the planet. The mean density of the satellite and the orbital semimajor axis are varied. The technical details of the simulations are described below.

2 NUMERICAL METHOD

The numerical simulations presented in this paper were conducted using the N -body integrator PKDGRAV (Stadel 2001). PKDGRAV is a parallelised hierarchical tree-code with a second-order leap-frog integrator. The satellite is assumed to be a rubble pile – a gravitational aggregate bound together by self-gravity (Richardson et al. 2002). A rubble pile by definition has no bulk tensile strength. However, the particles themselves that make up the rubble pile are rigid spheres and cannot interpenetrate or be crushed. As a result, the initial rubble-pile satellite has infinite compressional strength, some shear strength (due to interlocking particles), and some internal friction (Leinhardt et al. 2000). We have chosen to use a rubble-pile description for the initial satellites for two reasons: (i) Cordelia and Ophelia, the satellites on either side of the Uranian ϵ ring, are elongated, small bodies whose shape is consistent with that of a body held together purely by self-gravity (for Cordelia $R = 20$ km, ratio of shortest to longest axes is 0.7, Karkoschka 2001a); (ii) a rubble pile is the simplest internal structure we could model in a numerical study of the process of tidal disruption. The choice of initial satellite mass is largely arbitrary because the problem is essentially scale-free in the limit of small mass ratio.

The initial satellites are constructed from 4955 particles randomly placed in a low-density sphere in isolation (i.e., without a planetary gravitational potential). Self-gravity causes the particles to collapse toward the centre of the sphere. In order to damp collisional oscillations, the particle collisions are made highly inelastic ($\epsilon_n = 0.1$, see next paragraph; Leinhardt & Stewart 2012). This method of randomisation is favoured over hexagonal close packing (Leinhardt et al. 2000; Leinhardt & Richardson 2002), which generates a lattice structure that causes unrealistic results in both tidal disruption and collisional impacts.

¹ They state that $11,000 < Q_U < 39,000$, and we have $Q'_U = (3/2)Q_U/k_2$, where the Love number $k_2 = 0.104$ for Uranus.

The motion of each particle within the rubble-pile is governed by gravity and collisions. The inelastic collisions between particles are parameterised using the normal and tangential coefficients of restitution, ϵ_n and ϵ_t , respectively (Richardson 1994). In these simulations we omit surface friction by setting $\epsilon_t = 1$, as this would otherwise introduce an additional and poorly constrained parameter that does not have a significant effect on tidal disruption events (Richardson et al. 1998). The normal coefficient of restitution can vary between 0 (perfectly inelastic) and 1 (perfectly elastic) and determines the rebound velocity as the result of a collision. The relative velocity of two particles before their collision is

$$\mathbf{v} = \mathbf{v}_n + \mathbf{v}_t, \quad (2)$$

where \mathbf{v}_n is the component of \mathbf{v} normal to the impact surface and \mathbf{v}_t is the component tangent to the impact surface. The relative velocity after the collision is then

$$\mathbf{v}' = -\epsilon_n \mathbf{v}_n + \mathbf{v}_t. \quad (3)$$

The energy lost in a collision (to heat or minor deformation of the rubble pile constituents) is given by

$$\Delta E = -\frac{1}{2}\mu(1 - \epsilon_n^2)v_n^2, \quad (4)$$

where μ is the reduced mass of the particles involved in the collision.

Once the rubble piles have been successfully formed we model the inelastic collisions between particles with a higher coefficient of restitution, $\epsilon_n = 0.5$, which is consistent with results from laboratory impact experiments using ice, rock, and soil (Chau et al. 2002; Higa et al. 1996, 1998). In order to prevent inelastic collapse within the rubble piles, however, we set $\epsilon_n = 1$ for impacts with relative speeds less than 1% of the mutual escape speed. As a result the rubble-pile satellites have a low vibrational temperature.

We have chosen two simplistic internal structure models for the satellites: (i) a homogeneous body of uniform bulk density; (ii) a differentiated body consisting of two layers of different bulk densities. Disruption of a differentiated body may be able to produce one or two rings and a remnant satellite, as the denser core may resist tidal disruption at a semi-major axis where the lower-density mantle is stripped. The differentiated satellites have a density ratio of four between the core and mantle and a core size of about 35% by number (1714/4955). Since all the particles have the same size, the core particles are four times more massive than the mantle particles. This situation is more extreme than would be found in nature but has been chosen to make the results more straightforward to interpret. For both homogeneous and differentiated satellites we have investigated six mean densities from $0.5 - 3.0 \text{ g cm}^{-3}$ and a range of orbital semi-major axes in order to locate the onset of tidal disruption.

Once the model satellites have been formed they are placed in the gravitational potential of a central point mass (e.g., Uranus) in a circular orbit and in synchronous rotation. The system is then integrated for at least 100 orbits. In general the tidal disruption process is gentle and the particles within the rubble pile collide with each other slowly. As a result, we do not expect a large amount of damage or fracturing to the individual particles. Therefore, the rigid-

sphere model for the constituent rubble-pile particles is a reasonable approximation to reality.

3 RESULTS

We have divided our results into two sections: the first (§3.1) determines the conditions required for the disruption of a satellite, while the second (§3.2) describes the dynamics of the disruption and the formation of a ring system. We begin our discussion of the satellite disruption by quantifying the disruption criteria for satellites of varying mean densities and internal structure (§3.1.1). Subsequently, we discuss the various disruption paradigms our simulations exhibit, and connect them to appropriate analytical analogues, namely the evolution of a viscous fluid ellipsoid and the Roche-lobe overflow problem (§3.1.2). After the initial disruption phase, a proto-ring system forms, the global structure and evolution of which we relate to the different initial compositions of the disrupted satellite (§3.2).

3.1 Satellite Disruption

3.1.1 Disruption Criteria

Fig. 1 shows examples of the three types of tidal disruption that occur in the numerical simulations. The top row shows the full disruption of a homogeneous satellite. The initial change in shape takes several orbits; particles in the interior cannot move until particles on the surface have moved out of the way. Once the satellite has begun to elongate the disruption accelerates. The second row shows an example of a mantle disruption of a differentiated satellite. In this case only the surface layer particles are moving significantly. First the mantle changes into a lemon shape, then particles flow off the surface through the Lagrange points. This loss of mantle particles increases the mean density of the satellite as the core does not change shape significantly nor is there a significant change in the mean density of the core. Eventually a mean density is reached that is stable against tidal disruption and mantle particles are no longer lost from the surface. Note that the mantle stripping process observed here is comparable to that found in Canup (2010), implying that the dynamics of the disruption are common across a wide regime of gravity-dominated objects. The last row shows the full disruption of a differentiated satellite. Initially the mantle begins to disrupt in a similar but more vigorous fashion to the pure mantle disruption shown in the row above, with many particles flowing through the Lagrange points at once. However, the remnant is not dense enough in this case and the entire core shears out in a process that is similar to the disruption of the homogeneous satellite in the top row.

Tables 1 and 2 summarise how the tidal disruption of homogeneous and differentiated satellites depend on semi-major axis and bulk density. The result of the simulation is indicated by a D (full disruption; top and bottom rows of Fig. 1), MD (mantle disruption; middle row of Fig. 1), or N (no disruption) in the appropriate square. In cases of mantle disruption or no disruption the aspect ratio (ratio of shortest to longest axes) of the remnant is indicated under the disruption type. The axis ratios are determined by first identifying the particles within the rubble pile using

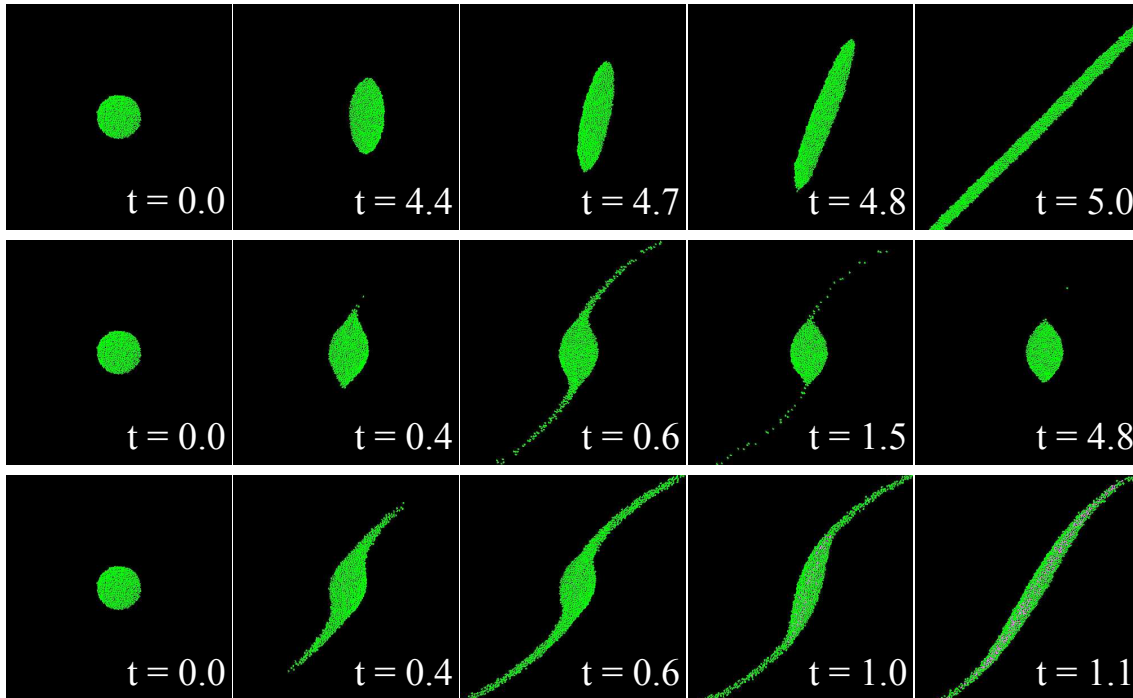


Figure 1. Examples of tidal disruption. The first row shows the full disruption of a homogeneous satellite ($\bar{\rho}_s = 0.5 \text{ g cm}^{-3}$, $a = 2.95 R_p$). The second is an example of mantle disruption for a differentiated satellite ($\bar{\rho}_s = 0.5 \text{ g cm}^{-3}$, $a = 2.55 R_p$). The third shows the full disruption of a differentiated satellite ($\bar{\rho}_s = 0.5 \text{ g cm}^{-3}$, $a = 2.36 R_p$). In the differentiated satellites the mantle particles are shown in green and the core particles are shown in magenta. Time increases from left to right and is shown in orbital periods. The images are in the rotating frame. 'Up' points radially away from the planet and 'down' points radially towards the planet and 'left' is along the orbit.

a clump-finding algorithm (Leinhardt et al. 2000) and then calculating the moment-of-inertia tensor of the rubble pile (Richardson et al. 1998).

The results are also presented graphically in Fig. 2. The relevant dimensionless parameter in this problem is the 'Roche parameter'

$$\mathcal{R} = \frac{\pi G \bar{\rho}_s}{\Omega^2} = \frac{3}{4} \frac{\bar{\rho}_s}{\bar{\rho}_p} \left(\frac{a}{R_p} \right)^3, \quad (5)$$

where $\bar{\rho}_s$ and $\bar{\rho}_p$ are the mean densities of the satellite and the planet, respectively, Ω and a are the angular velocity and the semi-major axis of the circular orbit, and R_p is the volumetric radius of the planet (25362 km for Uranus). For an incompressible fluid, tidal disruption occurs for $\mathcal{R} < 11.10$, where a solution in the form of a Roche ellipsoid can no longer be found (e.g. Chandrasekhar 1969); this condition corresponds to

$$\frac{a}{R_p} < 2.46 \left(\frac{\bar{\rho}_s}{\bar{\rho}_p} \right)^{-1/3}. \quad (6)$$

It is to be expected that rubble piles can survive to smaller values of \mathcal{R} than incompressible fluid bodies be-

cause of their shear strength. Indeed, for the homogeneous satellites we find a critical disruption distance that is closer to the planet than described by equation (6). We find a coefficient of about 2.2 instead of 2.46 (corresponding to a critical Roche parameter of about 7.7, as shown in Fig. 2). This coefficient is still larger than would be expected from the work of Holsapple & Michel (2006) and Holsapple & Michel (2008), which predicts a disruption coefficient of 1.7 for a homogeneous elongated body with an axis ratio of $\alpha = 0.7$, no tensile strength, and a friction angle of $\phi = 20^\circ$. We must be careful here because the criteria presented in Holsapple & Michel (2006) do not distinguish between a change in shape and true disruption; their calculations give only necessary conditions for disruption and not sufficient conditions. Therefore, perhaps the more reasonable comparison with Holsapple & Michel (2006) is to consider the critical distance within which the satellite necessarily departs from a sphere. We find that a rubble-pile satellite can maintain a spherical shape at a distance $a/R_p = (2.80 \pm 0.15) (\bar{\rho}_s/\bar{\rho}_p)^{-1/3}$. Within this limiting radius the rubble pile reshapes due to the tidal forces and transforms from a sphere into an ellipsoid. Thus, our rubble-

pile satellites behave somewhere in between a fluid and a rigid solid. Note that if the satellites were true fluids there would be *no* distance away from the central potential where a true spherical shape could be maintained. In this respect we are in agreement with Holsapple & Michel (2006) who also predict the existence of spherical equilibria outside a critical orbital radius. They find, however, that this radius is between 1.8 and 2.2 times $(\bar{\rho}_s/\bar{\rho}_p)^{-1/3}$ (for friction angles between 10 and 20 degrees). So there is a discrepancy of roughly 20–35%, which is acceptable given the uncertainties in their failure criterion and in its strict applicability to our numerical model.

The lower critical Roche parameter for the differentiated satellite can be explained, at least in part, by its greater central condensation. In the limit of a completely centrally condensed fluid satellite, the critical Roche parameter is approximately 6.25, which is significantly lower than the value of 11.10 for a homogeneous fluid body. The value 6.25 follows from the fact that the volume of the Hill sphere is approximately 1.509 Hill units (as determined by numerical integration).

3.1.2 Disruption Dynamics

Turning now to the dynamics of tidal disruption, we compare the outcomes of our N -body simulations of tidal disruption with two simplified analytical models. The disruption of a homogeneous satellite can be compared with the behaviour of a homogeneous viscous fluid ellipsoid which is described in detail below. On the other hand, the disruption of the mantle from an inhomogeneous satellite can be compared with Roche-lobe overflow which is described later in this section.

Homogeneous Satellite: Disruption of a Viscous Fluid Body

In this section we employ a simple fluid model that helps to illuminate the salient physics of satellite disruption. As Sridhar & Tremaine (1992, hereafter ST92) argue, a homogeneous rubble pile, exhibiting compressive and shear strengths but no tensile strength, can be crudely approximated by an incompressible viscous fluid ellipsoid. Under the influence of tidal forces, self-gravity, pressure, and viscous stresses, the shape and orientation of this ellipsoid can be computed with minimal effort, and its ultimate disruption reproduced. It is thus a convenient tool with which to interpret the more involved N -body simulations.

The formalism we use is that of ST92, and it consists of two sets of ordinary differential equations: the first, derived from the Navier–Stokes equations, describes the time-evolution of the constrained motions within the body; the second, derived from the boundary conditions, describes the evolution of the ellipsoidal geometry. Because we add little to the original formalism, these equations are not derived or listed: the reader is referred to their elegant presentation in ST92. The main difference is that our satellite is in a circular orbit at a fixed radius, not the parabolic orbit that ST92 examine. Consequently, the equations are solved in a corotating Cartesian frame centred upon the satellite that includes the Coriolis and centrifugal forces. We denote by Ω the orbital frequency at this radius, and the satellite is assumed to be initially spin-locked.

To approximate the internal friction of the rubble pile

a viscous stress is introduced with the dynamic viscosity proportional to the pressure. This mimics the expected increase in the shear stresses due to an applied pressure that is characteristic of most geological and granular materials (Holsapple & Michel 2006, 2008). Simply put, the more the rubble pile is ‘squeezed’, the greater its resistance to shear. Thus we have $\eta = \alpha(P/\Omega)$, where η is the dynamic viscosity, P is pressure, and α is a dimensionless parameter. There is a second parameter, the ‘Roche parameter’ $\mathcal{R} = \pi G \rho / \Omega^2$ introduced in Section 3.1.1, where ρ is the (constant) mass density of the satellite.

In order to compare with the N -body simulations, we set the distance between the satellite and Uranus to be $3R_p$ and take $\rho = 0.5 \text{ g cm}^{-3}$. This gives $\mathcal{R} = 7.57$ (well within the Roche limit). On the other hand, the viscosity parameter α is difficult to constrain, and we tried various values. But a higher $\alpha = 5$ yielded the best comparison. The initial state was usually a sphere.

In all our runs the evolution followed the same template: (a) a slow initial elongation of the body towards a roughly 2:1:1 configuration pointed at the planet, and then (b) a rapid extension in the azimuthal direction. Eventually the body transforms into a ‘needle’ with one of the principal axes of the ellipsoid orders of magnitude greater than the other two. This dominant axis is ultimately aligned with the azimuthal direction. Accompanying this change are non-linear oscillations in the internal motions, which may seed the growing perturbations observed in the N -body simulations (see §3.2 or Fig. 6 below). The viscosity parameter α strongly influences the slow first stage of the evolution: a large value can prolong this stage significantly. However, once the second shearing phase begins, the viscosity and pressure become unimportant and the fluid behaves more like a collection of ballistic particles.

In Fig. 3, we plot some snapshots of a typical evolution, to be compared with the first row of Fig. 1 describing the N -body simulations. The agreement between the two approaches is excellent and emphasises some interesting points. The peculiarities of the granular flow are unimportant in both stages of the evolution: in the first stage, all that matters is that there is some kind of internal friction, and its details are not essential; in the second stage, the particles behave ballistically and their collective dynamics is governed by the tidal force and the waning self-gravity force. Collisions are subdominant. What is striking, perhaps, is how far into the disruption the N -body simulation behaves like the incompressible fluid. The body does not break up into a ‘gaseous’ belt of relatively energetic particles – that comes later – but remains in a coherent closely packed ‘fluid’ phase for a substantial fraction of the ring formation. As is shown in §3.2 below, instabilities finally destroy this phase.

Differentiated Satellite: Roche-Lobe Overflow

Fig. 1 shows clearly that a differentiated satellite with a dense core behaves differently from a homogeneous satellite. In the case of the mantle disruption (middle row) the satellite becomes elongated into a lemon shape and then begins to lose mantle particles through the Lagrange points L1 and L2. The mass loss slows when the mean density of the satellite is high enough for the satellite to resist disruption (see also Canup 2010).

The motion of the ejected material can be modelled by considering the circular restricted three-body problem.

Table 1. Tidal disruption table for homogeneous satellites.

$\bar{\rho}$	$1.37 R_p$	$1.57 R_p$	$1.77 R_p$	$1.96 R_p$	$2.16 R_p$	$2.36 R_p$	$2.55 R_p$	$2.75 R_p$	$2.95 R_p$	$3.14 R_p$	$3.34 R_p$	$3.54 R_p$
0.5							D	D	D	$\frac{N}{0.74}$	$\frac{N}{0.82}$	$\frac{N}{0.88}$
1.0				D	D	$\frac{N}{0.55}$	$\frac{N}{0.77}$	$\frac{N}{0.86}$				
1.5			D	D	$\frac{N}{0.7}$	$\frac{N}{0.82}$	$\frac{N}{0.91}$					
2.0		D	D	$\frac{N}{0.71}$	$\frac{N}{0.84}$	$\frac{N}{0.90}$	$\frac{N}{0.92}$					
2.5	D	D	$\frac{N}{0.67}$									
3.0	D	D	$\frac{N}{0.81}$									

Table 2. Tidal disruption table for differentiated satellites.

$\bar{\rho}$	$1.18 R_p$	$1.37 R_p$	$1.57 R_p$	$1.77 R_p$	$1.96 R_p$	$2.16 R_p$	$2.36 R_p$	$2.55 R_p$	$2.75 R_p$
0.5							D	$\frac{MD}{0.56}$	$\frac{N}{0.64}$
1.0				D	$\frac{MD}{0.53}$	$\frac{N}{0.64}$			
1.5			D	$\frac{MD}{0.56}$	$\frac{N}{0.74}$				
2.0		D	$\frac{MD}{0.59}$	$\frac{N}{0.73}$					
2.5		D	$\frac{N}{0.54}$	N					
3.0	D	$\frac{MD}{0.58}$	$\frac{N}{0.76}$						

In these calculations we use the same mass ratio as in the N -body simulations. Particles are started at rest close to the Lagrangian points L1 and L2 so that they accelerate away from the Roche lobe (or Hill sphere) and approach Keplerian orbits far from the satellite. The trajectories are plotted in the frame that rotates with the two-body orbit in Fig. 4. In this frame the particles nearly come to rest once per orbital period. Eventually the particles encounter the satellite again.

This calculation can also be done within the Hill approximation, in which case the final state of the ejected particles (not allowing for any subsequent encounter with the satellite) is an epicyclic motion with an amplitude of 3.08 Hill radii and a guiding centre displaced by 4.96 Hill radii from the orbit of the satellite. The motion therefore extends from 1.88 to 8.04 Hill radii.

A zoomed-out view of the N -body simulation of mantle disruption is shown in Fig. 5. In a frame rotating with the satellite’s orbit, the streams of ejected particles form rounded scallop shapes as they trace out the trajectories of the three-body problem described above. The density of the tidal streams is enhanced at the locations where the particles nearly come to rest and trajectories turn around. Here the particles collide with one another and their individual trajectories are changed (see second and third frame of Fig. 5). By the last frame in Fig. 5 the mass loss from the mantle has reduced significantly. Particles collide much less frequently and the scallop shape becomes cleaner.

As shown in the last row of Fig. 1, a differentiated satellite that is close enough to the planet will be fully disrupted. This process shows characteristics of both the disruption of

the homogeneous satellite and the mantle disruption discussed above. At first the mantle material flows off of the satellite at locations close to the Lagrange points but the stream created by the mantle particles is much thicker than in the mantle-only disruption event. Once most of the mantle is removed, the core also disrupts and stretches out into an elongated needle similar to the disruption of the homogeneous satellite.

3.2 Ring Formation and Ring Properties

As remarked in Section 3.1.2, the initial disruption of the homogeneous satellite is remarkably ordered, consisting of the rapid shearing-out of the body into a coherent, needle-like ellipsoid. However, after some time, this ellipsoid (or proto-ringlet) is attacked by a secondary gravitational instability, the evolution of which is described in Fig. 6. The complete disruption of the differentiated satellite follows a similar evolution. The instability kinks the ringlet into a jagged ribbon on small scales, eventually destroying its coherence through physical collisions or gravitational encounters. Gravitational potential energy is injected into random motions and the ringlet spreads, becoming a ‘hot’ belt of particles. Because of the distinct kink-like morphology of the unstable mode, it is probably not of the same class as the longitudinal instability that attacks a self-gravitating cylinder (described by Chandrasekhar 1961). It may be, however, related to the non-axisymmetric instabilities of thin incompressible rings and tori calculated by various authors (see Cook & Franklin 1964; Goodman & Narayan 1988; Papaloizou & Lin 1989; Christodoulou & Narayan 1992; Latter et al. 2012). What

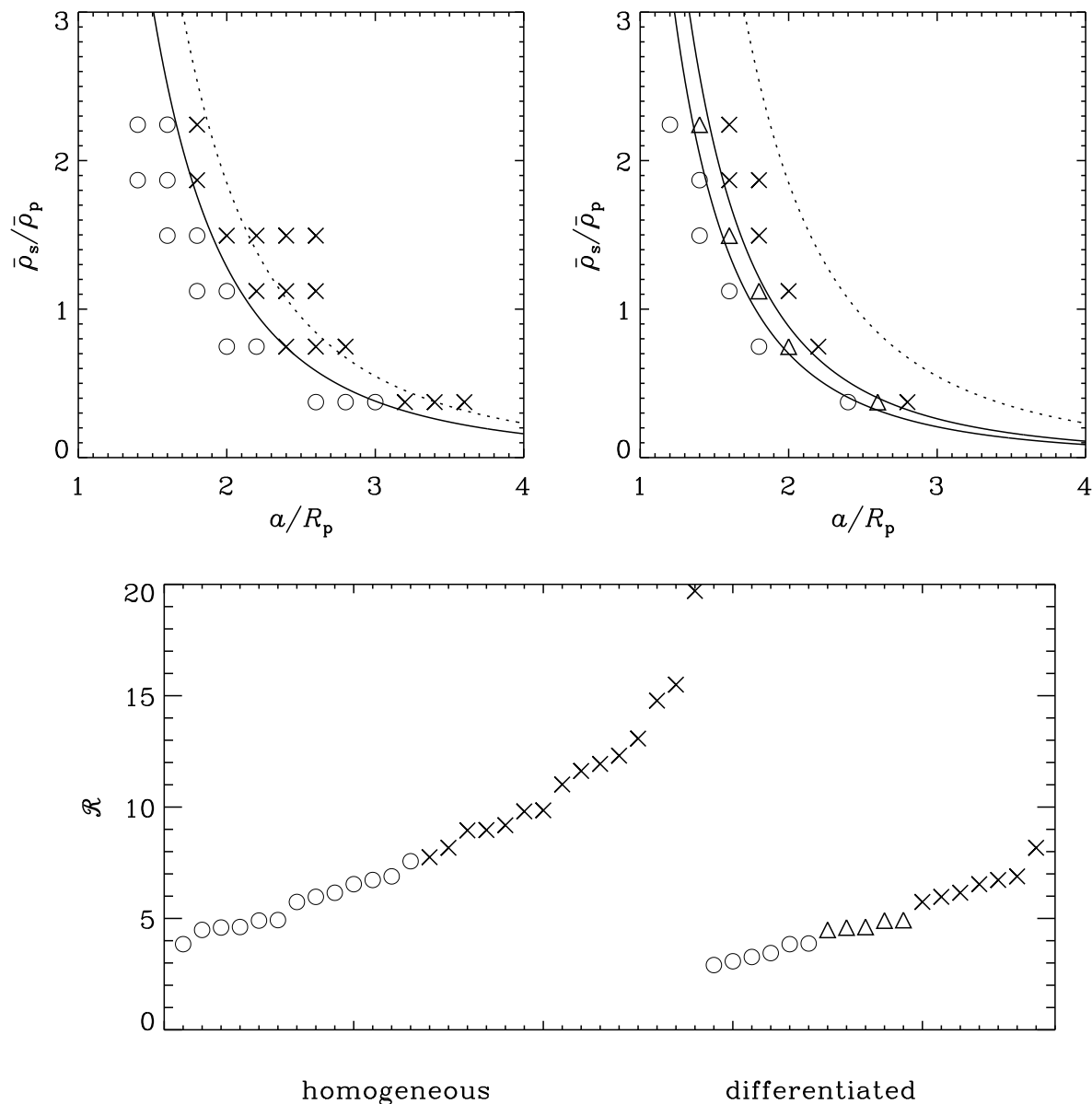


Figure 2. Tidal disruption of satellites. Top left: Outcome of numerical simulations of homogeneous satellites for various ratios of orbital semi-major axis to planetary radius and various ratios of satellite density to planetary density. ○ indicates full tidal disruption, while × indicates no disruption. The dotted line shows the Roche limit for an incompressible fluid body, $\mathcal{R} = 11.10$, while the solid line shows $\mathcal{R} = 7.7$. Top right: Similar results for differentiated satellites. Here △ indicates mantle disruption only and the two solid lines show $\mathcal{R} = 4.2$ and $\mathcal{R} = 5.3$. Bottom: Results expressed in terms of the Roche parameter.

is interesting is that the deterioration of the homogeneous satellite into a disordered and collisional belt of particles is a two-stage process: first an ordered shearing-out into a coherent ellipsoidal-like body of ‘cold’ particles, and then the disruption of this body by a secondary instability that rips up the ordered object into an incoherent collisional belt.

In order to get a more global picture of the longer-term ring evolution let us look at the ring in polar coordinates rotating with the satellite’s orbit (Fig. 7). Note that the evolution shown in Fig. 6 occurs while the disrupted satellite is still an incomplete ring. In the case of the homogeneous satellite (top row), the ring arc continues to grow in azimuth until it wraps around, eventually forming a spiral structure.

There is a periodic sinusoidal pattern due to the eccentricity of the particle streams, which results from the original location of the particles in the satellite. However, in the case of the mantle disruption of the differentiated satellite (middle row), the periodic stream structure is destroyed by the remnant core. The mantle particles are scattered by the core at every encounter. In the full disruption of the differentiated satellite (bottom row), the core particles show the same wrapping periodic pattern of the homogeneous satellite. The mantle particles, on the other hand, show much less of a coherent pattern because the core did not disrupt immediately. Thus, some of the mantle particles were scattered by a still coherent core.

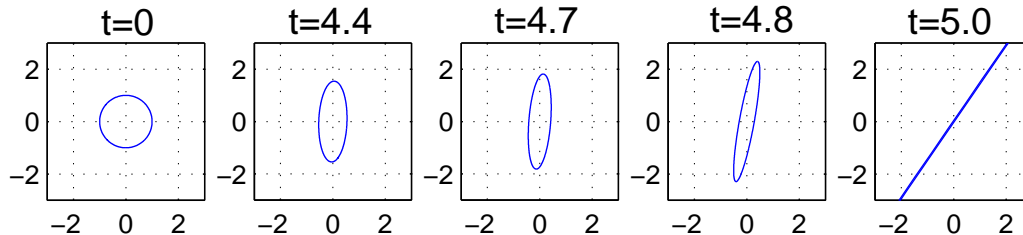


Figure 3. Four snapshots of the evolution of a viscous fluid body within its Roche limit, as computed by the ST92 model in a circular orbit. The Roche parameter is $\mathcal{R} = \pi G\rho/\Omega^2 = 7.57$ and the alpha viscosity parameter is $\alpha = 5.0$. The times are in orbital periods but the unit of length is arbitrary. ‘Down’ is towards the planet, and ‘left’ is along the circular orbit. The initial state is a sphere. This figure should be compared with the first row of Fig. 1.

We now discuss the dynamical state of the newly formed rings. Each particle can be considered to execute an elliptical Keplerian orbit, interrupted infrequently by collisions or gravitational encounters with other ring particles or the remnant satellite. The orbital properties of greatest interest are the specific angular momentum and the eccentricity.

The specific angular momentum of a ring particle can be expressed in terms of the radius of the guiding centre of its epicyclic motion, $r_g = (L_z/m)^2(GM_p)^{-1}$, where L_z is the z component of angular momentum and m is the mass of the particle. Fig. 8 shows the guiding-centre radius of the particles as a function of the initial radial location within the satellite. We have subtracted from each of these the radius of the initial satellite orbit so that the disruption of satellites initially placed at different radial locations can easily be compared with each other on the same axes. The change in global slope of the mantle particles is due to the initial re-equilibration of the rubble pile before disruption. Note in the middle row the core maintains its original slope which is an indication that the core has stayed spherical and has not re-equilibrated. This is also initially the case in the full

disruption of the differentiated satellite. Note the change in slope of the core particles lags behind the change in slope of the mantle particles. However, by the second orbit the core has deformed and subsequently fully disrupted. The diffusion of the initial line of particles to a “fatter” distribution is the result of the inter-particle scattering. This diffusion can also be seen in the top row of Fig. 9, which shows the number of particles as a function of guiding centre position. Over time the distribution of particles broadens and the peak particle number at the centre of the ring drops smoothly.

In the mantle disruption of the differentiated satellite the particles are released from L1 and L2 but they then interact gravitationally with the remaining core creating the lopsided bow-tie structure seen in last frame of the middle row of Fig. 8. Initially the mantle disruption shows up as a double-horned feature in Fig. 9 but as the particles interact with the core the peaks broaden into wings in the overall number density distribution (last frame).

In the full disruption of the differentiated satellite the evolution of the particles is a bit confused as some of the mantle particles seem to be released from L1 and L2 but

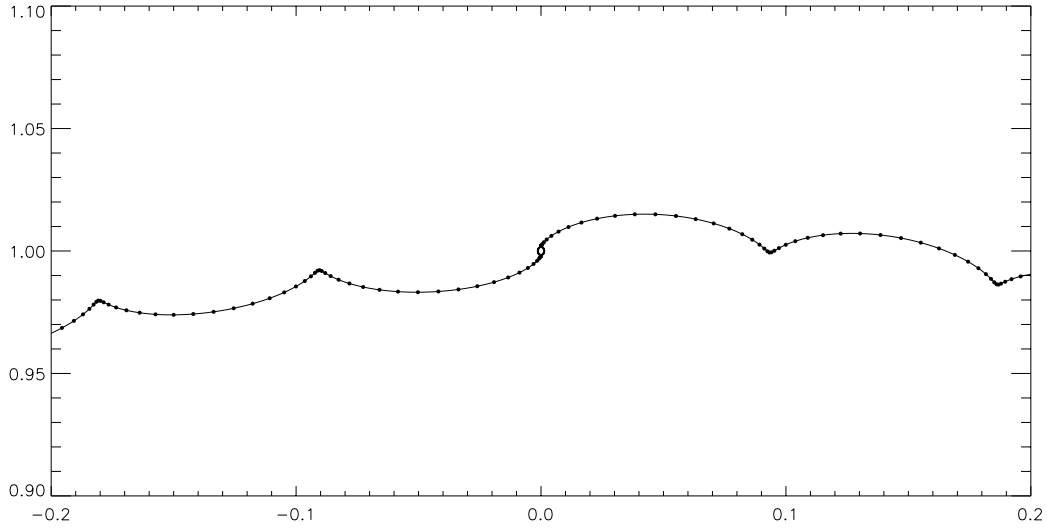


Figure 4. Trajectories of particles in the circular restricted three-body problem that start at rest close to the Lagrangian points L1 and L2. Twenty particle positions per orbital period are superimposed on the trajectories, and the Roche lobe is also shown. The mass ratio is 2.335×10^{-8} . Coordinates are referred to the central mass and are in units of the orbital separation.

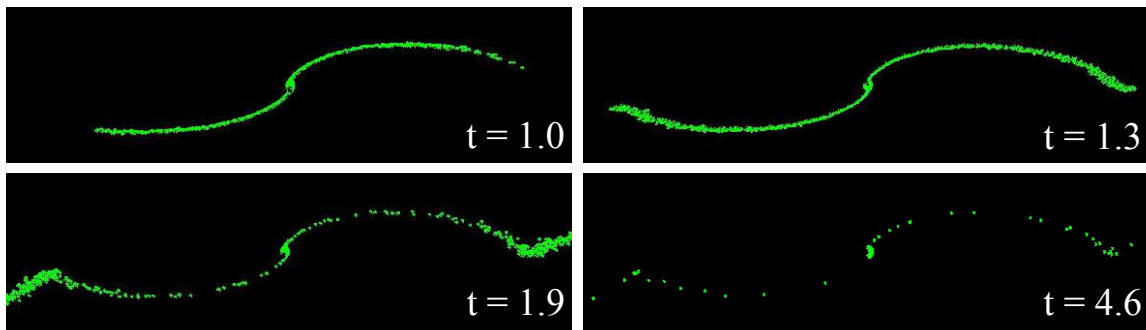


Figure 5. Zoomed-out view of the same simulation shown in the second row of Fig. 1. The frame is ~ 0.3 units of the orbital separation in length, ~ 340 Hill radii of the original satellite (1 Hill radius ~ 70 km). The sizes of particles have been inflated by a factor of ten in order to make them more visible. This figure should be compared with Fig. 4.

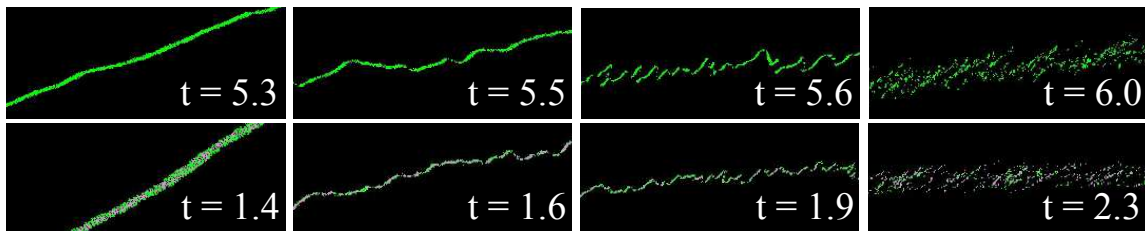


Figure 6. Snapshots of the formation of rings from two fully disruptive simulations. These frames follow on from the first and third rows of Fig. 1: the top row is for a homogeneous satellite and the bottom row is for a differentiated satellite in which the denser core particles are coloured magenta. In the top row the frames from left to right have lengths of 13, 26, 53 and 53 Hill radii of the original homogeneous satellite. In the bottom row the frames have lengths of 16, 33, 66, and 66 Hill radii of the original differentiated satellite. The size of the frames was chosen to have the same physical size (1000, 2000, 4000, and 4000 km).

the core and remaining mantle material follow a disruption path that is similar to the homogeneous satellite shown in the top row. For example, the third frame of the last row in Fig. 9 looks like a combination of the mantle disruption and the total disruption described above, with the double-peaked structure of the mantle particles and the broad structure of the disrupted core. However, this horned feature disappears and ring spreads. By 100 orbits the distribution of particles in the ring looks like the homogeneous disruption shown in the top row. In both the mantle disruption and the total disruption of the differentiated satellite we can see evidence of ring spreading and inter-particle scattering.

The eccentricity vector and epicyclic amplitude, shown in Fig. 10 and Fig. 11, respectively, show the initial dynamical state of the newly formed ring in each type of disruption event and reveal the extent of the interactions between ring particles. The homogeneous satellite produces a distribution in Fig. 10 with the total extent of e_y equal to about half the total extent of e_x , where $e_x = e \cos \varpi$ and $e_y = e \sin \varpi$ (ϖ is the longitude of pericentre), and preserves the characteristic “v” shape in the epicyclic amplitude, suggesting that the particles have not interacted with each other after the

disruption. Interestingly the linear anomaly seen in the last frame in the top row is due to an undisrupted rubble-pile chunk that survived the tidal disruption. In this particular simulation the initial satellite was closer to the critical Roche limit than the other simulations allowing a chunk of material to remain gravitationally intact.

The mantle-only disruption produces eccentricity components that have the same range (in the x and y components of the eccentricity vector in Fig. 10) suggesting interaction and angular momentum exchange between mantle particles. In addition, the epicyclic amplitude shows many more particles outside of the characteristic “v” indicating significant interaction with the remnant core.

Finally, the full disruption of the differentiated satellite shows a combination of the two results. The core material looks vaguely like the homogeneous satellite in Fig. 10 and Fig. 11 with a rough two-to-one relationship between e_y and e_x and a ‘v’ shape in epicyclic amplitude and guiding centre position. The mantle material, on the other hand, is uniformly distributed in eccentricity between -0.01 and 0.01 and shows a broad range of epicyclic amplitude and guid-

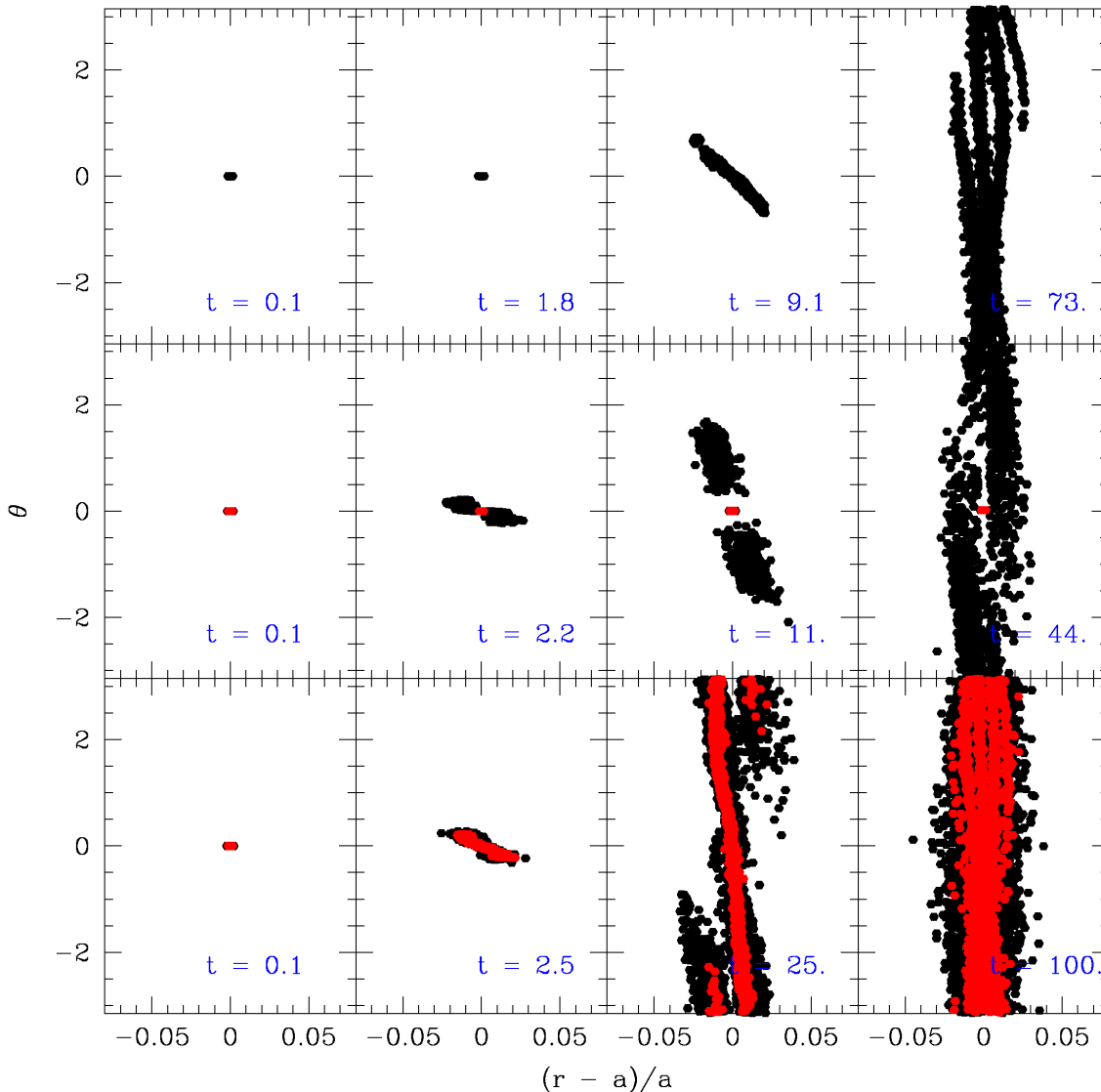


Figure 7. Ring particle locations in polar coordinates rotating with the satellite’s orbit. The core particles are shown in red. The x axis shows the radial positions of the ring particles with respect to the initial location of the satellite, a . The three rows correspond to the three simulations shown in Fig. 1: the top row is the full disruption of a homogeneous satellite, the middle row is the mantle disruption of a differentiated satellite, and the bottom row is the full disruption of a differentiated satellite.

ing centre position. This is a result of mantle particles being scattered by the remnant and disrupting core.

4 DISCUSSION & CONCLUSION

4.1 Summary

As all the planets in the outer solar system have ring systems, we are deeply interested in their formation and evolution. In this paper we have investigated the formation of narrow rings through the tidal disruption of a weak, gravitationally bound satellite that migrates within its Roche limit. In our N -body numerical simulations, the satellite is modelled as a rubble pile: a gravitational aggregate of spherical particles that undergo inelastic collisions. We have considered both homogeneous satellites and differentiated

bodies, the latter being composed of denser core particles surrounded by a less dense mantle.

We have shown that the Roche limit for a rubble pile is closer to the planet than for a fluid body of the same mean density, although its location scales in the same way with the mass of the planet and the mean density of the satellite. The Roche limit for a differentiated body is also closer to the planet than for a homogeneous satellite of the same mean density.

Within its Roche limit, a homogeneous satellite is totally disrupted and forms a narrow ring. The initial stages of the disruption are similar to the evolution of a viscous fluid ellipsoid, which becomes highly elongated in the azimuthal direction. Later, gravitational instability produces irregular structure and dynamics within the proto-ringlet.

On the other hand, a differentiated satellite tends to un-

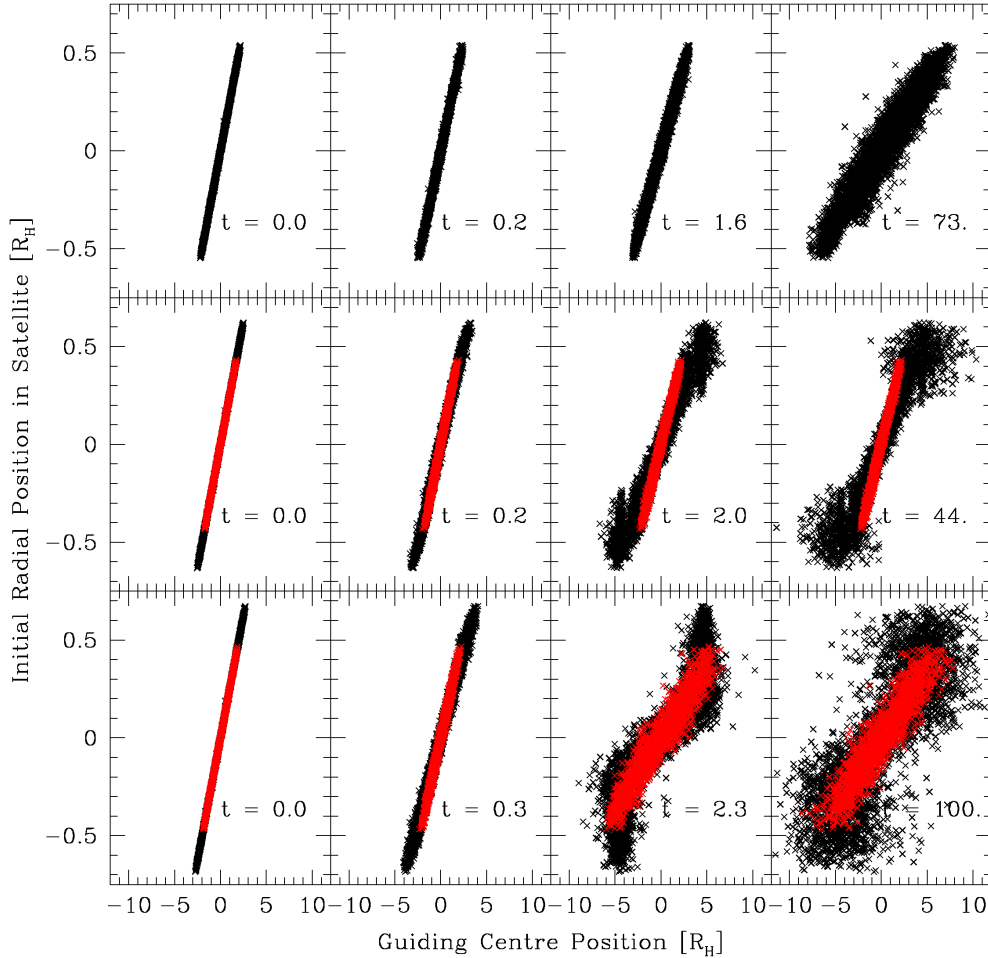


Figure 8. The original location of particles in the initial satellite versus the guiding centre position of the particles in the ring in units of the Hill radii of the original satellite. The core particles are indicated in red. The three rows correspond to the three different types of disruption shown in Fig.1.

dergo a disruption of its mantle only. This process is similar to Roche-lobe overflow in interacting binary stars, although proceeding simultaneously through both Lagrange points L1 and L2, and produces streams of ejected particles whose trajectories are initially well described by solutions of the restricted three-body problem. Again, however, gravitational instability affects the streams near nodes where the particles come almost to rest in the corotating frame and the density is enhanced. This type of disruption process produces two narrow rings on either side of a remnant satellite. If a differentiated satellite is placed sufficiently close to the planet, however, it undergoes a total disruption which has features of both the processes described above.

In future work we will consider the evolution of the narrow rings and attendant satellites formed by these mechanisms.

4.2 Application to Specific Ring Systems

Our results suggest that narrow rings such as those found around Uranus could have formed by tidal disruption as opposed to the generally favoured mechanism of disruption by external impact. Depending on the properties of the original

satellite, tidal disruption can form either a single ring or two narrow rings with a remnant satellite in between. Similarly, disruption of a number of inwardly migrating satellites could produce a chain of narrow rings, possibly interspersed with remnant satellites.

To date, shepherding by satellites is the only known mechanism of maintaining the sharp edges of narrow rings as observed around Uranus and Saturn. Only one of Uranus' rings (the ϵ ring) has known shepherds, and even in this case there are theoretical difficulties in accounting for the survival of the configuration (Goldreich & Porco 1987). If the rest of the rings in the Uranian system have shepherds they must be small and dark. We suggest that the elusive shepherds, if present, could be either the undisrupted cores of differentiated satellites that suffered a mantle disruption, or small undisrupted satellites that were either dense enough or strong enough to resist tidal disruption.

Tidal disruption of a pre-existing satellite may be responsible for the formation of some or all of the rings found around planets in our solar system. The satellite must first migrate within its Roche limit; this could come about through tidal interaction with the planet, if the satellite orbits within the corotation radius of the planet, or through

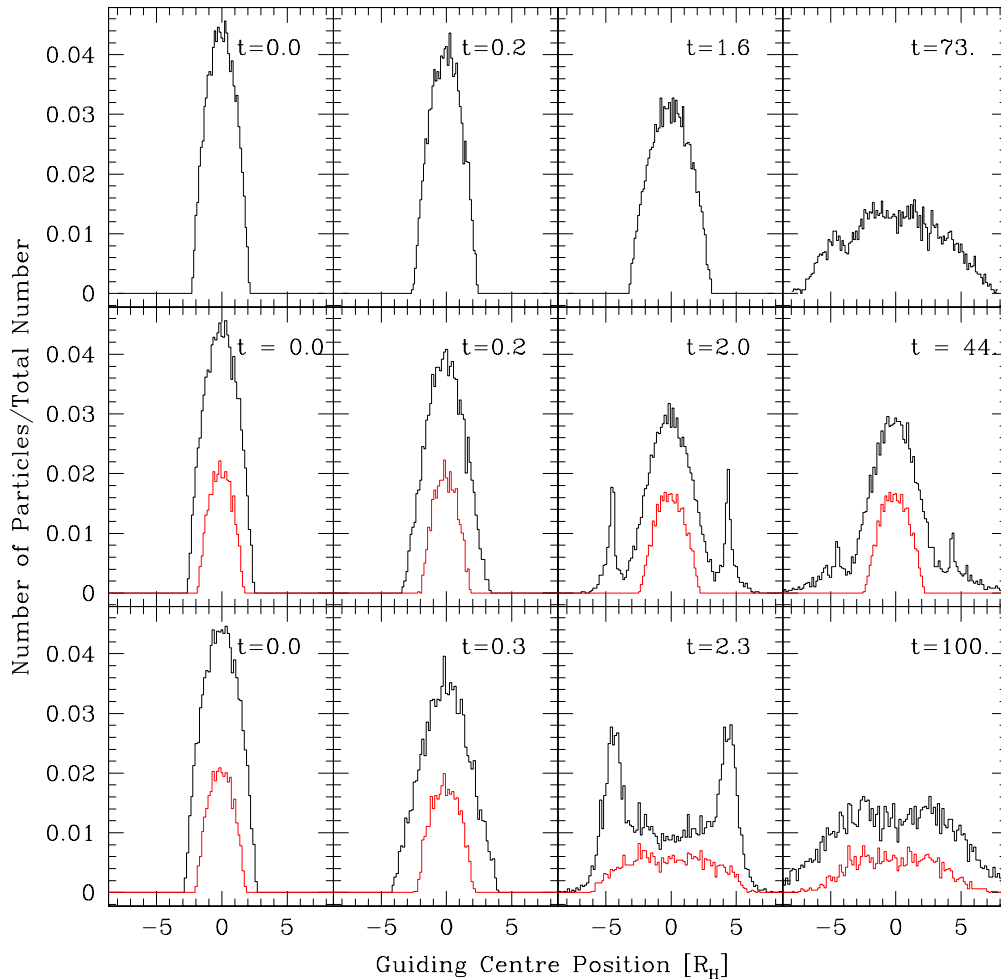


Figure 9. Histograms of the guiding centre position. The black line indicates all particles, while the red line is for core particles only.

planet-disk interaction in the early evolution of the system. For the smaller ice giant planets Uranus and Neptune the Roche limit (assuming a homogeneous fluid body with a density of 1 g cm^{-3}) lies inside the corotation radius, which means that satellites that were formed between these two radii would migrate inwards through tidal interaction with the planet and eventually be disrupted to form rings. This zone occupies roughly 67000–83000 km for Uranus and 71000–84000 km for Neptune. The process would be ongoing until the reservoir of satellites was depleted, but is very slow because of the long time-scale of tidally induced migration. These successive tidal disruptions could explain the many narrow rings found in the Uranian system if there was originally a significant reservoir of small satellites between the Roche limit and the corotation radius; there are currently eleven known moons of Uranus inside corotation.

For the gas giant planets the Roche limit (calculated with the same assumptions) is outside the corotation radius, which suggests that tidal interaction with the planet could only lead to outward migration and so could not be responsible for ring formation. However, the regular satellites of the

gas giants are expected to form in a circumplanetary gas disk. While the gas is present it could have caused inward migration leading to ring formation through either partial or total tidal disruption as suggested by Canup (2010). Indeed, inward type I migration is thought to be sufficiently rapid that it may be difficult to explain the retention of any proto-satellites while the gas remains. We note, however, that these comparisons of the corotation radius and Roche radii are uncertain. The corotation radius is expected to decrease with time as a result of the contraction of the planet and the reduction of its moment of inertia. Also, as we have shown, the Roche radius for a rubble pile is smaller than for a fluid body, and the Roche limit of a centrally condensed body is smaller than for a homogeneous one. Therefore it is conceivable the corotation radius may have exceeded the appropriate Roche limit in the past (as suggested by Canup 2010) and that tidal migration may therefore have led to ring formation around Jupiter and Saturn as well.

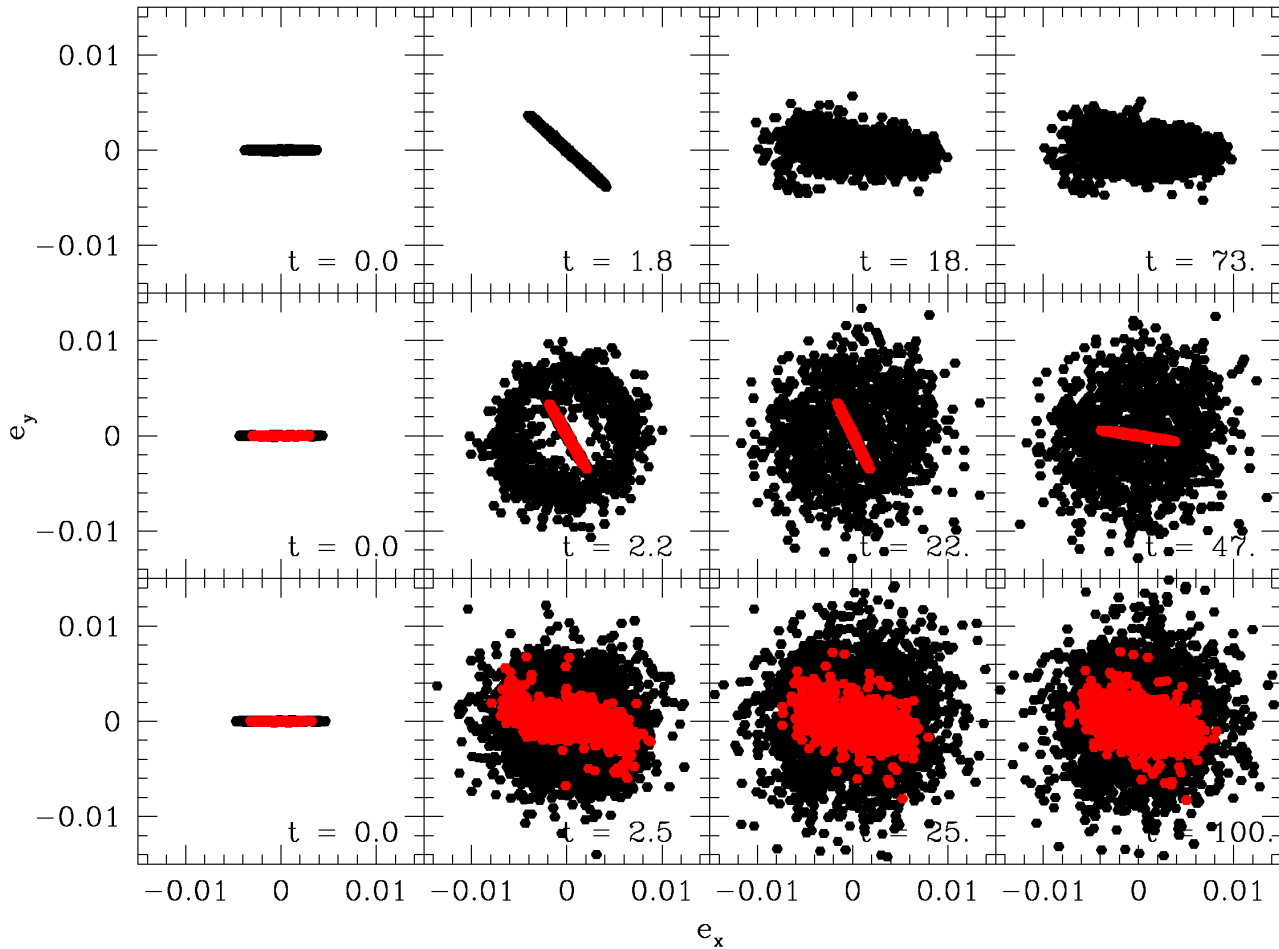


Figure 10. Evolution of the eccentricity vectors for all particles versus time. The core particles are indicated in red.

ACKNOWLEDGEMENTS

The authors thank an anonymous referee for fast and constructive feedback. This research was supported by an STFC Rolling Grant and by a Royal Society Joint Project with Japan. ZML is currently supported by an STFC Advanced Fellowship.

REFERENCES

- Broadfoot A. L. et al., 1986, *Science*, 233, 74
 Burns J., Hamilton D. P., Showalter M. R., 2001, *Dusty Rings and Circumplanetary Dust: Observations and Simple Physics*. Springer, pp 641–725
 Canup R. M., 2010, *Nature*, 468, 943
 Chandrasekhar S., 1961, *Astrophysical Journal*, 134, 662
 Chandrasekhar S., 1969, *Ellipsoidal figures of equilibrium*
 Charnoz S., Dones L., Esposito L., Estrada P., Hedman M., 2009, in Dougherty M., Esposito L., Krimigis S., eds, *Saturn from Cassini-Huygens Origin and evolution of saturn’s ring system*. Springer, pp 537–575
 Charnoz S., Morbidelli A., Dones L., Salmon J., 2009, *Icarus*, 199, 413
 Chau K. T., Wong R. H. C., Wu J. J., 2002, *International Journal of Rock Mechanics and Mining Sciences*, 39, 69
 Christodoulou D. M., Narayan R., 1992, *ApJ*, 388, 451
 Cook A. F., Franklin F. A., 1964, *Astronomical Journal*, 69, 173
 Dones L., 1991, *Icarus*, 92, 194
 Esposito L., 2006, *Planetary Rings*
 Esposito L. W., Brahic A., Burns J. A., Marouf E. A., 1991, *Particle properties and processes in Uranus’ rings*. pp 410–465
 Goldreich P., Porco C. C., 1987, *AJ*, 93, 730
 Goldreich P., Soter S., 1966, *Icarus*, 5, 375
 Goodman J., Narayan R., 1988, *MNRAS*, 231, 97
 Harris A., 1984, in Greenberg R., Brahic A., eds, *Planetary Rings The origin and evolution of planetary rings*. University of Arizona Press, pp 641–659
 Higa M., Arakawa M., Maeno N., 1996, *Planet. Space Sci.*, 44, 917
 Higa M., Arakawa M., Maeno N., 1998, *Icarus*, 133, 310
 Holsapple K. A., Michel P., 2006, *Icarus*, 183, 331
 Holsapple K. A., Michel P., 2008, *Icarus*, 193, 283
 Karkoschka E., 1997, *Icarus*, 125, 348
 Karkoschka E., 2001a, *Icarus*, 151, 51
 Karkoschka E., 2001b, *Icarus*, 151, 78

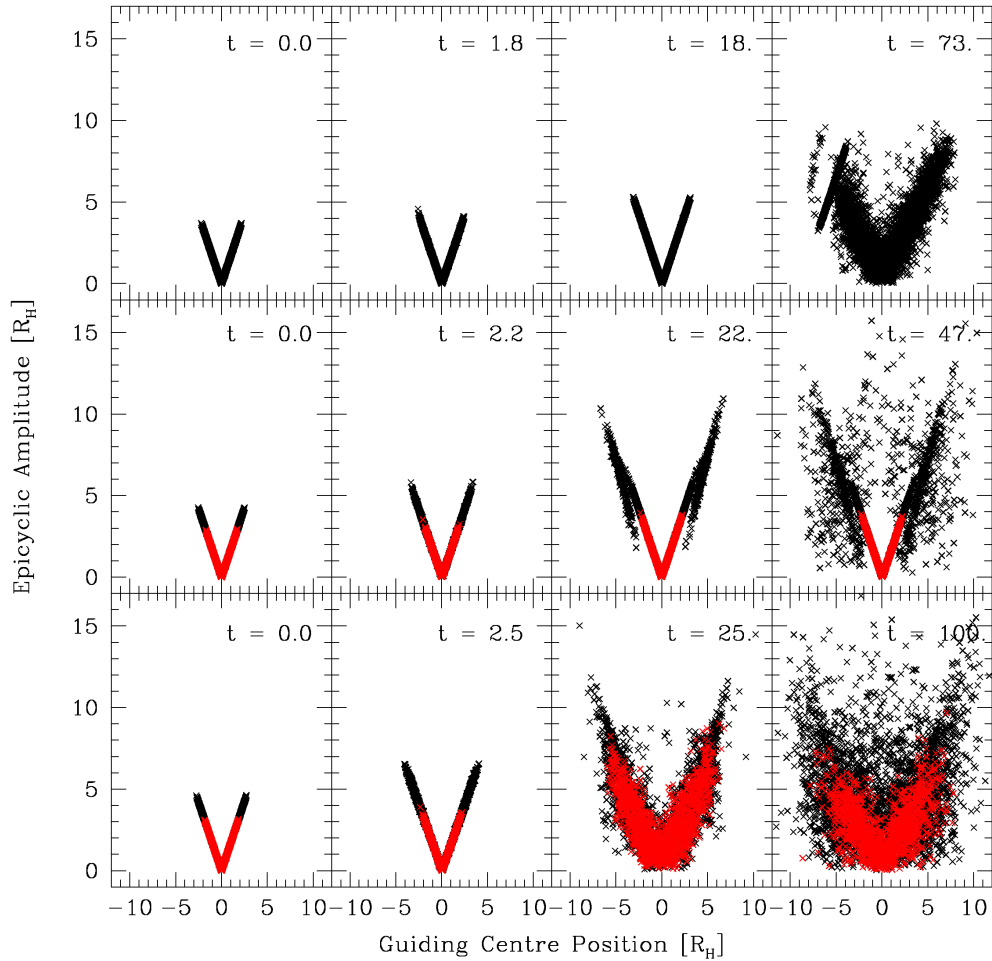


Figure 11. Epicyclic amplitude versus guiding centre position. Red indicates core particles.

Latter H., Rein H., Ogilvie G. I., 2012, *Monthly Notices of the Royal Astronomy*
 Leinhardt Z. M., Richardson D. C., 2002, *Icarus*, 159, 306
 Leinhardt Z. M., Richardson D. C., Quinn T., 2000, *Icarus*, 146, 133
 Leinhardt Z. M., Stewart S. T., 2012, *ApJ*, 745, 79
 Ockert M. E., Cuzzi J. N., Porco C. C., Johnson T. V., 1987, *J. Geophys. Res.*, 92, 14969
 Ogilvie G. I., Lin D. N. C., 2004, *ApJ*, 610, 477
 Papaloizou J. C. B., Lin D. N. C., 1989, *ApJ*, 344, 645
 Pollack J. B., 1975, *Space Sci. Rev.*, 18, 3
 Porco C. C., 1990, *Advances in Space Research*, 10, 221
 Richardson D. C., 1994, *MNRAS*, 269, 493
 Richardson D. C., Bottke W. F., Love S. G., 1998, *Icarus*, 134, 47
 Richardson D. C., Leinhardt Z. M., Melosh H. J., Bottke Jr. W. F., Asphaug E., 2002, *Asteroids III*, pp 501–515
 Showalter M. R., 1993, in *AAS/Division for Planetary Sciences Meeting Abstracts #25* Vol. 25 of *Bulletin of the American Astronomical Society*, Longitudinal Variations in the Uranian Lambda Ring. p. 1109
 Showalter M. R., Lissauer J. J., 2006, *Science*, 311, 973
 Sridhar S., Tremaine S., 1992, *Icarus*, 95, 86
 Stadel J. G., 2001, PhD thesis, UNIVERSITY OF WASH-

INGTON
 Tittlemore W. C., Wisdom J., 1990, *Icarus*, 85, 394